processes

MDPI

Article

Multi-Objective Design Optimization of Serpentine Liquid-Cooled Plates Based on CFD and Hybrid Surrogate Modeling

Shuo Ma, Qingtong Liu *, Wenting Liu, Mantuo Li and Xinyu Hong

School of Mechanical and Automotive Engineering, Liaocheng University, Liaocheng 252000, China; mashuo_1101@163.com (S.M.); liuwenting@lcu.edu.cn (W.L.); bywwhite1@163.com (M.L.); xinyuhong163@163.com (X.H.)

* Correspondence: liuqingtong@lcu.edu.cn; Tel.: +86-188-1152-8689

Abstract

This study proposes a multi-objective optimization strategy for the structural design of liquid-cooled channels in battery systems, aiming to identify liquid-cooled plate design schemes with better cooling performance and acceptable flow resistance. Optimal Latin hypercube sampling (OLHS) was combined with computational fluid dynamics (CFD) simulations to construct a CFD-generated dataset that includes the maximum temperature and system pressure drop. Then, modeFRONTIER was employed to integrate surrogate-model training, rapid prediction, and non-dominated sorting genetic algorithm II (NSGA-II) optimization, thereby obtaining the Pareto optimal set. The technique for order preference by similarity to ideal solution (TOPSIS) decision method was further introduced to determine the final optimal design. Results indicate that the optimized liquid-cooling system exhibits outstanding comprehensive performance in terms of balancing heat dissipation and flow resistance at a 5 C discharge rate. Remarkably, sensitivity analysis shows that inlet velocity is the dominant factor affecting the maximum battery temperature, with a correlation coefficient of −0.789. The maximum temperature of the battery module is effectively limited to 30.07 °C, while the flow pressure drop is only 799.58 Pa, achieving an excellent balance between heat dissipation efficiency and energy consumption.

Keywords: battery thermal management system (BTMS); multiobjective optimization; NSGA-II; CFD; hybrid surrogate model

Check for updates

Academic Editor: Li Xi

Received: 12 May 2026
Revised: 7 June 2026
Accepted: 8 June 2026
Published: 10 June 2026

Copyright: © 2026 by the authors. Licensee MDPI, Basel, Switzerland. This article is an open access article distributed under the terms and conditions of the Creative Commons Attribution (CC BY) license.

1. Introduction

In the context of global energy transformation and carbon reduction, the research and development of new energy technologies has become the core strategy for countries to deal with energy security and environmental challenges [1–3]. As the main power source of new energy vehicles, lithium-ion batteries (LIBs) have become the mainstream choice for electrochemical energy storage systems [4,5]. This dominant position is attributed to their high energy density, excellent cycle stability and extremely low self-discharge rate. However, there is a significant coupling relationship between the electrochemical performance and operating temperature of LIBs. Excessive operating temperature will significantly accelerate the degradation of active substances, and this thermal stress will inevitably shorten the battery life [6]. Under extreme conditions of heat dissipation failure, such high temperatures may also induce catastrophic thermal runaway, leading to serious safety accidents such as fire or explosion [7]. These thermal safety issues have become

major technical barriers, limiting the performance of power batteries and hindering the large-scale commercial application of electric vehicles (EVs) [8]. Hence, it is imperative to develop an efficient battery thermal management system (BTMS). The system is very important to maintain the battery pack within the optimal temperature range, so as to improve the reliability, safety and life of the vehicle.

In order to achieve accurate thermal regulation, the integration of a BTMS into electric vehicle battery packs is indispensable. At present, air cooling and liquid cooling are the two main technical paths of thermal management. At the same time, to further enhance the heat dissipation performance, some emerging cooling technologies have also been widely studied, including heat pipe cooling, phase change material cooling, and thermoelectric cooling [9,10].

Air cooling is favored by manufacturers and widely used in BTMSs due to its low manufacturing cost, high system reliability, and absence of leakage risks. Kirad and Chaudhari [11] revealed the decoupling mechanism of the spacing parameter, proving that the transverse spacing dominates the cooling efficiency, while the longitudinal spacing determines the temperature uniformity. Feng et al. [12] used a variety of design of experiments (DOE) methods to jointly optimize the discrete and continuous parameters, and confirmed that the best cooling performance can be obtained by combining the inlet channel angle of 4° with the spacing of 2.5 mm. Moosavi et al. [13] observed that although increasing the spacing ratio can reduce the temperature difference, it will lead to an increase in the maximum temperature, which highlights the limitations of single-parameter design and the necessity of collaborative optimization. Gao et al. [14] suppressed the wake effect by integrating an inclined splitter plate, which reduced the pressure drop and temperature difference by 11.9% and 49.2%, respectively, and realized the deep synergy of thermal performance and hydraulic performance. Finally, Lyu et al. [15] used genetic algorithms (GAs) to optimize the layout of deflectors and batteries, which proved that the temperature rise was reduced by 30% and the temperature difference was reduced by 80%, which verified the potential of structural topology reconstruction.

Under high-rate discharge conditions, the efficiency of air-cooling will be fundamentally restricted due to its poor thermal performance. Therefore, the liquid-cooling scheme has become an inevitable choice for high-performance systems. Even so, liquid cooling still faces performance bottlenecks; that is, the improvement of heat transfer performance will lead to an increase in pumping costs. This limitation has prompted the current research direction toward the precise design of the channel topology. Jiang et al. [16] analyzed the joint heat dissipation laws of nanofluids and phase change materials and found that an increase in duct height can cause a significant temperature drop, which highlights the core role of geometric optimization in enhancing the thermal response of multi-physics systems. Based on orthogonal experiments and double-sided cooling topologies, Bao and Shao et al. [17] proposed an ultra-thin wide straight channel to overcome the limitations of fluid resistance, and confirmed that the structure can effectively suppress temperature rise and temperature difference while significantly reducing pumping power consumption. Zhang et al. [18] used the inclined channel structure to reshape the flow field, which improved the overall energy efficiency by 79.64% compared with the traditional configuration at an inclination of 15°. Finally, Kong et al. [19] proposed a dual-inlet and single-outlet divergent channel configuration, which confirmed that the topology reduced the pressure drop by 7.2% and decreased the temperature difference to 3.19 K.

Serpentine channels are widely used in large battery thermal management systems because of their excellent structural reliability, manufacturing simplicity and space compactness. In order to further expand the performance boundary of this configuration, recent research has given priority to the refinement of structure and the integration of functions.

For example, Kanjirakat et al. [20] transformed the design into a three-dimensional architecture, achieving a 32.9% reduction in peak temperature and a 77.7% improvement in thermal uniformity. To solve the restriction between flow resistance and cooling demand, Liu et al. [21] successfully combined the serpentine architecture with encapsulated phase change materials and an intelligent fuzzy control strategy, reducing energy consumption by more than 70%. These recent developments show that the thermal and hydraulic performance of the classic serpentine layout can be substantially improved through targeted topology and operation optimization.

Although the research on battery thermal management has made great progress, most of the existing work focuses on the specific configuration or material improvement, and there is still a gap in the systematic exploration of multi-objective collaborative optimization mechanisms. The key to the multi-objective collaborative optimization mechanism lies in balancing the intrinsic relationship between temperature control indicators and system pressure drop. However, there is a complex nonlinear mapping relationship between design variables and optimization objectives, which is also the reason why traditional empirical methods cannot adapt to multi-objective collaborative optimization mechanisms.

To demonstrate more clearly the characteristics and limitations of existing liquid-cooled BTMS optimization research, Table 1 summarizes and compares representative studies. Here, computational fluid dynamics (CFD), liquid-cooled plate (LCP), optimal Latin hypercube sampling (OLHS), non-dominated sorting genetic algorithm II (NSGA-II), and technique for order preference by similarity to ideal solution (TOPSIS) are used to describe the main components of the optimization framework proposed in this paper.

Table 1. Comparison of representative BTMS optimization studies and the present work.

Study	Cooling Structure	Method	Surrogate Strategy	Objectives	Key Feature
Ding et al. [22]	Liquid-cooling channels	Parametric analysis	Not reported	Maximum temperature and temperature uniformity	Channel shape and aspect-ratio effects
Zhao et al. [23]	Liquid-cooled plate	Structural optimization	Not reported	Maximum temperature and temperature uniformity	LCP structural-parameter optimization
Fan et al. [24]	Tree-like cooling plate	Parametric optimization	Not reported	Maximum temperature, temperature uniformity, and pressure drop	Bionic tree-like channel design
Zhang et al. [25]	Topology-optimized cold plate	Topology optimization	Not reported	Cooling performance and pressure drop	Topology-enhanced thermal-hydraulic performance
Dai et al. [26]	Parallel-serpentine channels	CFD optimization	Not emphasized	Cooling performance and pressure drop	Parallel-serpentine channel integration
Fan et al. [27]	Secondary-flow serpentine plate	Numerical investigation	Not reported	Cooling performance and pumping power	Secondary-channel-enhanced serpentine flow
Vishwakarma and Rana [28]	Serpentine cold plate	Computational parametric analysis	Not reported	Cooling performance and pressure loss	Geometric effects on serpentine channels
Mubashir et al. [29]	Single/double serpentine plates	Experimental and numerical investigation	Not reported	Maximum temperature, temperature difference, and parasitic power	Single- vs. double-serpentine comparison
Present work	**Serpentine liquid-cooled plate**	**CFD + OLHS + NSGA-II + TOPSIS**	**Hybrid surrogate model**	**Maximum temperature and pressure drop**	**Thermal-hydraulic trade-off optimization**

Contributions

Following the above research background, this study established a three-dimensional CFD model of a serpentine liquid-cooled plate. Afterwards, a hybrid optimization frame-

work combining response surface methodology (RSM), NSGA-II, and TOPSIS was constructed to optimize the liquid-cooling plate geometry and inlet flow velocity parameters.

The main contributions of this study are summarized as follows:

- A three-dimensional CFD model of a serpentine liquid-cooled plate was established and partially validated against experimental data reported in [30] under 1.5 C discharge conditions.
- A surrogate-model-assisted multi-objective optimization framework integrating RSM, NSGA-II, and TOPSIS was proposed to improve optimization efficiency while balancing thermal performance and hydraulic resistance.
- The competitive relationship between heat dissipation performance and pressure-drop characteristics was quantitatively analyzed, providing theoretical guidance for the design of high-efficiency and low-resistance BTMS.

This study elucidates the competitive evolution logic between heat dissipation performance and energy consumption cost, providing key support for the sustainable development of new energy vehicle power batteries throughout their entire lifecycle.

2. Materials and Methods

In this section, a 15 Ah capacity lithium iron phosphate ($LiFePO_4$) lithium-ion battery (LIB) was used as the main research object. Table 2 summarizes the relevant parameters of the battery and sets 45 °C as the maximum safe operating temperature during the operation of the battery. For the internal structure of liquid-cooled plates, serpentine liquid-cooled plates (LCPs) have efficient heat transfer due to their simple structure and large heat exchange area, which facilitates dissipating heat from the battery surface. In order to match the physical dimensions of lithium batteries, various aluminum plates have been developed to meet thermal management requirements.

Table 2. Detailed specifications of the $LiFePO_4$ LIB cell [30].

Parameters	Values
Nominal capacity	15 Ah
Nominal voltage	3.2 V
Product size	18 mm × 140 mm × 65 mm
Over-discharge protection voltage	2.25 V
Weight	0.35 kg
Overcharge protection voltage	3.65 V
Continuous discharge current	3 C
Instantaneous discharge current	5 C
Specific heat capacity	1633 J/(kg·K)
Thermal conductivity	$\lambda_x = \lambda_y = 29$ W/(m·K) $\lambda_z = 1$ W/(m·K)

2.1. Geometrical Model

The power battery pack consists of several battery modules connected in series or parallel. As shown in Figure 1a, the structure of each module is composed of multiple cells and liquid-cooled plates arranged in a row. The specific parametric model of the liquid-cooled plate can be observed in Figure 1b. Although d_1, d_2, d_3, and d_4 define the fixed physical dimensions of the cell and liquid-cooling plate, the cooling performance of the liquid-cooling plate is mainly controlled by four adjustable design variables: geometric parameters such as channel width (l), channel height (h), and spacing (s), as well as hydraulic parameters such as inlet velocity (v). Since the combined effects of these parameters directly determine the thermohydraulic performance and heat dissipation efficiency of the

cooling system, these parameters have been identified as key targets for optimizing the system's heat dissipation performance in the future.

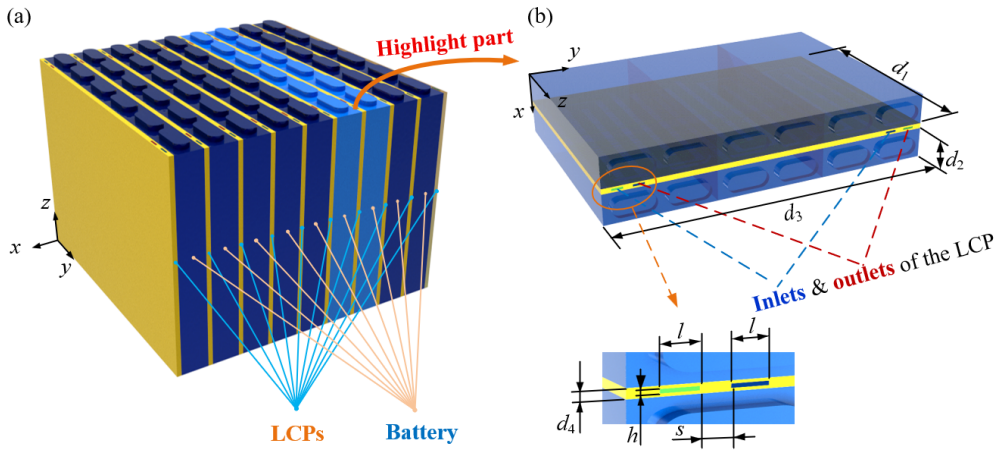


Figure 1. (**a**) Assembly of the battery module and the selection of the computational unit; (**b**) Geometry and parametric definitions of the simplified liquid-cooling model.

Based on the effect of the serpentine symmetrical flow channel, the design focus of the internal structure of the serpentine liquid-cooling plate is to maximize the heat dissipation area under geometrical constraints. Based on these design principles, this study developed two flow channel design schemes with different inlet and outlet layouts, as shown in Figure 2. Case 1 and Case 2 are, respectively, the same side serpentine circuit and the opposite side serpentine circuit, ensuring the combination effect of the inlet and outlet of the serpentine liquid-cooling plate, which can better exert the heat dissipation effect of the serpentine liquid-cooling plate. The main body of the liquid-cooled plate is made of aluminum, and its structural integrity and reliability are ensured through stamping and welding processes. Considering that the cooling system needs to have stable thermophysical properties, this study selected a 50% ethylene glycol aqueous solution as the cooling liquid. The combined action of the liquid-cooling plate and coolant enables precise temperature control of Li-ion battery modules. The key parameters regarding material properties and coolant performance at 20 °C are shown in Table 3.

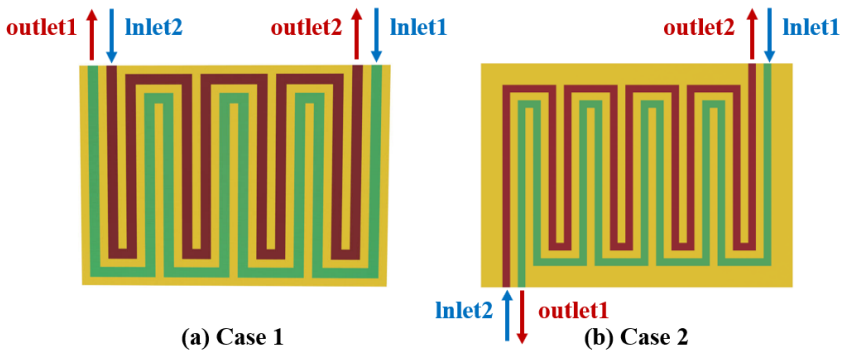


Figure 2. Schematic of the liquid-cooling plate internal channel structures: (**a**) Case 1 (same-side) and (**b**) Case 2 (opposite-side).

Table 3. Physical property parameters of materials.

Material Name	Density (kg/m^3)	Specific Heat Capacity (J/(kg·K))	Thermal Conductivity (W/(m·K))
Aluminum	2707	903	237
Ethylene glycol aqueous solution	1071	3319	0.464
Silicone pad	6000	920	15

2.2. Mathematical Model

CFD was employed to analyze the fluid flow and heat transfer in the liquid-cooled battery module. The fluid was assumed to be an incompressible Newtonian fluid with constant thermophysical properties. In the numerical model, the fluid flow field was governed by the conservation equations of mass, momentum, and energy, while heat transfer inside the battery cell was described using a transient heat conduction equation [31,32]. The mass conservation equation for the fluid flow is expressed as follows:

$$\frac{\partial \rho}{\partial t} + \frac{\partial (\rho u)}{\partial x} + \frac{\partial (\rho v)}{\partial y} + \frac{\partial (\rho w)}{\partial z} = 0, \tag{1}$$

where ρ denotes the fluid density; u, v, and w represent the fluid velocity components in the x, y, and z directions, respectively; and t indicates time.

For the fluid discussed in this study, assuming constant density and incompressibility, Equation (1) can be simplified as follows:

$$\frac{\partial u}{\partial x} + \frac{\partial v}{\partial y} + \frac{\partial w}{\partial z} = 0. \tag{2}$$

The incompressible fluid flow in the cooling channel is governed by the Navier–Stokes equations. The momentum conservation equation is expressed as follows:

$$\rho\left(\frac{\partial \mathbf{u}}{\partial t} + \mathbf{u} \cdot \nabla \mathbf{u}\right) = -\nabla p + \nabla \cdot \left[(\mu + \mu_t)\left(\nabla \mathbf{u} + \nabla \mathbf{u}^T\right)\right], \tag{3}$$

where $\mathbf{u}$ is the velocity vector, p is the pressure, μ is the dynamic viscosity, and μ_t is the turbulent viscosity.

The energy conservation equation is used to describe the convective and conductive heat transfer processes of the fluid in the cooling channel. The specific mathematical description is as follows:

$$\begin{aligned} &\frac{\partial (\rho T)}{\partial t} + \frac{\partial (\rho u T)}{\partial x} + \frac{\partial (\rho v T)}{\partial y} + \frac{\partial (\rho w T)}{\partial z} \\ &= \frac{\partial}{\partial x}\left(\frac{k}{C_p}\frac{\partial T}{\partial x}\right) + \frac{\partial}{\partial y}\left(\frac{k}{C_p}\frac{\partial T}{\partial y}\right) + \frac{\partial}{\partial z}\left(\frac{k}{C_p}\frac{\partial T}{\partial z}\right) + S_T, \end{aligned} \tag{4}$$

where T is the temperature; k is the thermal conductivity of the fluid; C_p is the specific heat capacity; and S_T represents the viscous dissipation term in the fluid energy equation.

In the Reynolds-averaged Navier–Stokes (RANS) framework, we chose the standard k-ϵ model mainly because it is very stable when calculating large-scale regions and has a fast convergence speed. The transport equations corresponding to turbulent kinetic energy (k) and dissipation rate (ϵ) are as follows[33]:

$$\frac{\partial (\rho k)}{\partial t} + \frac{\partial (\rho u_i k)}{\partial x_i} = \frac{\partial}{\partial x_j}\left[\left(\mu + \frac{\mu_t}{\sigma_k}\right)\frac{\partial k}{\partial x_j}\right] + G_k - \rho\epsilon, \tag{5}$$

$$\frac{\partial(\rho\epsilon)}{\partial t} + \frac{\partial(\rho u_i \epsilon)}{\partial x_i} = \frac{\partial}{\partial x_j}\left[\left(\mu + \frac{\mu_t}{\sigma_\epsilon}\right)\frac{\partial \epsilon}{\partial x_j}\right] + C_{1\epsilon}\frac{\epsilon}{k}G_k - C_{2\epsilon}\rho\frac{\epsilon^2}{k}, \quad (6)$$

where G_k represents the production of turbulent kinetic energy; μ_t denotes the turbulent viscosity; σ_k and σ_ϵ are the turbulent Prandtl numbers for k and ϵ, respectively; and $C_{1\epsilon}$ and $C_{2\epsilon}$ are empirical constants.

A three-dimensional transient heat conduction model is established to describe the internal energy transfer within the LIB [34]. This model incorporates anisotropic thermal conductivity to accurately resolve the temperature field evolution, accounting for the complex internal structure of the cell. The governing equation is expressed as:

$$\rho C_p \frac{\partial T}{\partial t} = \lambda_x \frac{\partial^2 T}{\partial x^2} + \lambda_y \frac{\partial^2 T}{\partial y^2} + \lambda_z \frac{\partial^2 T}{\partial z^2} + Q, \quad (7)$$

where ρ and C_p denote the average density and specific heat capacity of the battery, respectively; T represents the battery temperature; t is the time; λ_x, λ_y, and λ_z are the thermal conductivities in the x, y, and z directions, respectively; and Q indicates the volumetric heat generation rate.

Determining the volumetric heat generation rate accurately remains challenging due to the diverse and complex factors influencing this core parameter for thermal simulations. Accordingly, the energy balance equation proposed by Bernardi [35] is adopted in this study, as follows:

$$Q = \frac{I}{V_b}\left[(E - U) + T\frac{dE}{dT}\right], \quad (8)$$

where I denotes the charge/discharge current; V_b indicates the battery volume; E and U refer to the open-circuit voltage (OCV) and operating voltage, respectively; T is the battery temperature; and dE/dT is defined as the entropic heat coefficient.

Given its negligible magnitude, the contribution of the entropic heat term is ignored in the calculations. Furthermore, according to Ohm's law, the voltage drop $(E - U)$ is equivalent to the product of the discharge current I and the internal equivalent resistance R (i.e., $E - U = IR$). Substituting this relationship into the equation, the formula is simplified as:

$$Q = \frac{I}{V_b}(E - U) = \frac{I^2 R}{V_b}. \quad (9)$$

where R denotes the internal equivalent resistance of the battery, and the unit for the volumetric heat generation rate Q is unified as W/m^3 throughout this study. Specific volumetric heat generation rates under various discharge rates, derived from experimental measurements [30], are summarized in Table 4.

Table 4. Volumetric heat generation rates of the LIB at different discharge rates.

Discharge Rate (C)	Heat Generation Rate (W/m^3)
1	15,935
3	80,771
5	189,563

2.3. Meshing and Validation Process

ANSYS Fluent 2024 R2 was used for numerical simulation to study the dynamic characteristics of the system's heat dissipation. The computational domain is discretized into 697,288 grid cells. When generating a polyhedral mesh, the volume growth rate is set to 1.2, and a three-layer prism layer grid (boundary layer) is generated at the interface

between fluid and solid. To directly resolve the viscous sublayer, local mesh refinement was carried out in the near-wall region, keeping the average y^+ value around 0.46. As shown in Figure 3, to display the details of grid division and the grid configuration of the inlet and outlet more clearly, this study extracted a representative volume element (REV) for display.

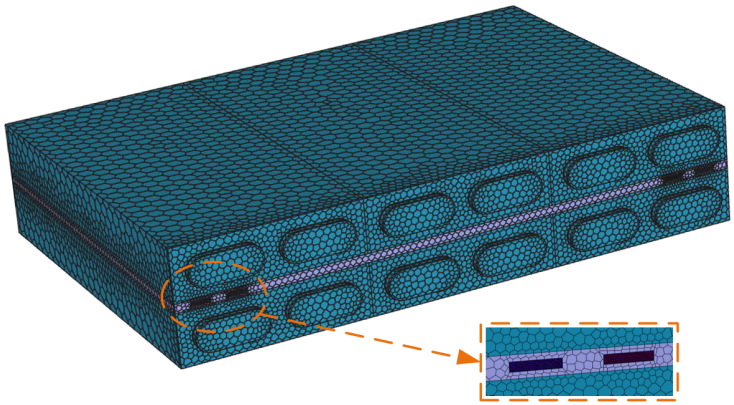


Figure 3. Polyhedral mesh topology of the REV extracted from the battery module, featuring a zoomed-in view of the boundary layer grids at the channel cross-section.

For the steady-state CFD simulations, the coolant inlet was defined as a velocity-inlet boundary condition, with the velocity specified as the magnitude normal to the boundary. Since the inlet velocity v was selected as one of the DOE design variables, its value was assigned according to each sampled case. The outlet was defined as a pressure-outlet boundary condition with a gauge pressure of 0 Pa. The coolant inlet temperature was set to 20 °C. The external surfaces of the computational domain were subjected to natural convection with a heat transfer coefficient of 5 W/(m^2·K) and a free-stream temperature of 300 K. At the internal fluid–solid interfaces, coupled thermal boundary conditions were applied to ensure the continuity of temperature and heat flux. The battery heat release was implemented as a uniform volumetric energy source in the solid battery-cell domain, and the heat generation rate was assigned according to Table 4. The computational domain was initialized at 300 K. The residual convergence criteria were set to 10^{-6} for the energy equation and 10^{-3} for the continuity, momentum, turbulent kinetic energy, and turbulent dissipation rate equations. The standard k-ϵ turbulence model parameters were kept at their default values: $C_\mu = 0.09$, $C_{1\epsilon} = 1.44$, $C_{2\epsilon} = 1.92$, $\sigma_k = 1.0$, $\sigma_\epsilon = 1.3$, $Pr_t = 0.85$, and $Pr_{wall} = 0.85$.

In addition, this study conducted a grid independence test to ensure the accuracy of numerical calculations. Three sets of polyhedral meshes with different densities were simulated and verified at a discharge rate of 5 C, and the quantitative results are summarized in Table 5. The results show that the maximum temperature calculated maintains high stability at all grid density levels. The maximum temperature among the three mesh levels remained stable, while the pressure drop deviation significantly decreased from 10.59% between the coarse and medium meshes to 1.23% between the medium and fine meshes. Meanwhile, the temperature deviation between the medium mesh and the fine mesh was only 0.27%. Considering this deviation, taking into account the accuracy of numerical calculations and the requirements for iterative operations of subsequent algorithms, the "medium grid" configuration was ultimately chosen as the optimal computational grid. Figure 4 displays the corresponding grid distributions across the three evaluated mesh levels.

Table 5. Quantitative results of the grid independence study. Note: δ_T and δ_P denote the relative deviations of maximum temperature and pressure drop between two adjacent mesh levels, respectively.

Mesh Level	Number of Cells	T (°C)	P (Pa)	δ_T (%)	δ_P (%)
Coarse	318,203	30.09	714.91	0.07	10.59
Medium	**697,288**	**30.07**	**799.58**	**0.27**	**1.23**
Fine	1,006,323	29.99	809.51	–	–

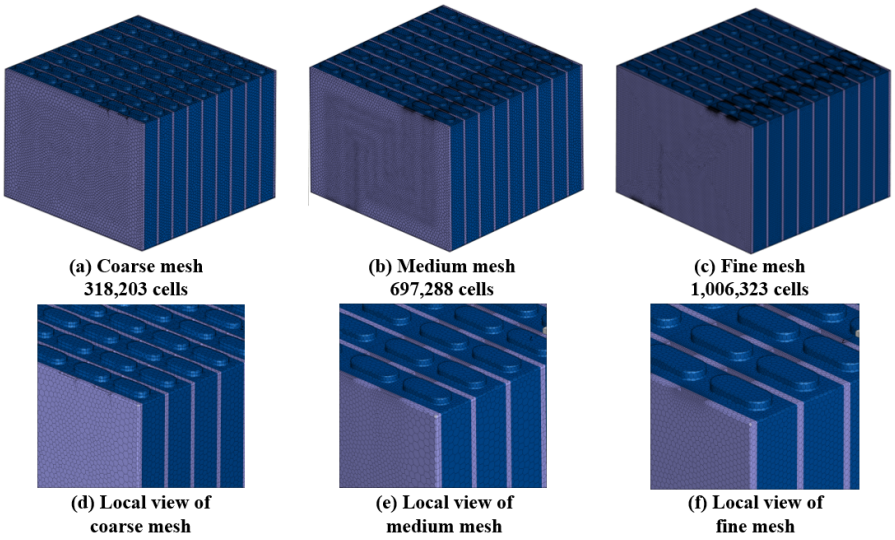


Figure 4. Global and local views of the coarse, medium, and fine meshes with corresponding cell counts.

Based on the above numerical model framework, the transient thermal characteristics of a single cell under 1.5 C discharge were studied. For the transient validation simulation, a fixed time-step method was adopted, with a physical time-step size of 1 s and a maximum of 20 iterations per time step. The total simulation time was set to 1500 s to capture the temperature evolution during the discharge process. As shown in Figure 5, by recording the temperature rise and heat distribution at three typical time steps, it can be observed that the maximum temperature shows a monotonically increasing trend with time, rising from 303.83 K at 500 s to 310.40 K at 1500 s. The temperature contours also show that the heat accumulation rate in the core area of the battery cell is greater than the heat dissipation rate on the battery surface. Therefore, the simulation results shown in Figure 5 provide a reliable physical basis for evaluating the performance of the cooling system under continuous operating conditions.

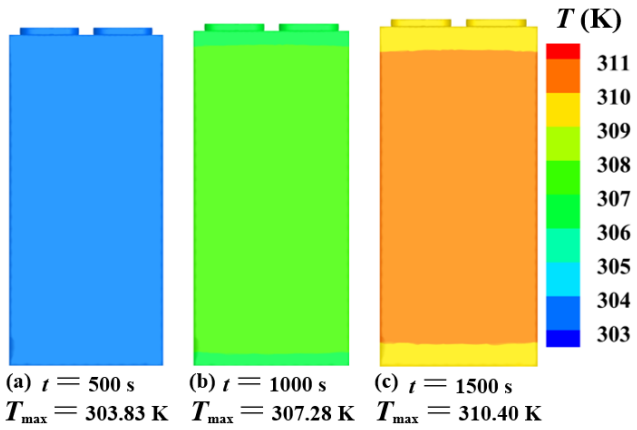


Figure 5. Transient temperature field evolution for the battery cell at: (**a**) 500 s, (**b**) 1000 s, and (**c**) 1500 s.

As a validation of the transient thermal simulation results of the single cell, the simulated temperature curve under the 1.5 C discharge condition was compared with the corresponding experimental data [30], and the error distribution curve between the simulated and experimental values was obtained, as shown in Figure 6. During this limited discharge cycle, transient discharge testing causes the system to exhibit a continuous heating dynamic thermal behavior. To rigorously quantify the computational bias during this transient process, this study extracted the global statistical error of the entire transient evolution process. Statistical evaluation shows that the maximum absolute error during the entire transient process does not exceed 0.92 °C, and the maximum relative error is as low as 2.3%. In addition, the root-mean-square error (RMSE) is 0.42, which further verifies the high prediction accuracy of the numerical model under dynamic conditions.

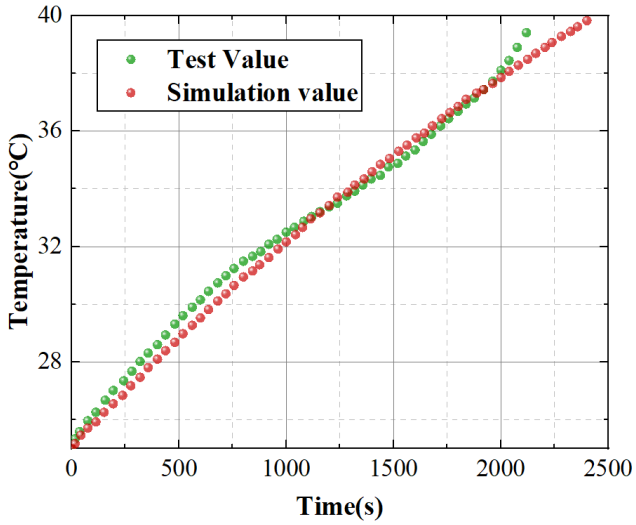


Figure 6. Comparison of simulated transient temperature profiles with experimental data reported in [30] at 1.5 C discharge.

2.4. Surrogate Modeling and Multi-Objective Optimization Framework

Figure 7 shows an integrated optimization architecture that combines high-precision response surface surrogate models with multi-objective evolutionary algorithms. Owing to the complex nonlinear coupling between geometric variables and thermodynamic indices, it is often difficult to obtain the global optimal solution within a limited timeframe using traditional analytical methods or large-scale numerical simulations. Thus, in the initial stage of this study, RSM was introduced as a surrogate model to address time-consuming numerical calculations. Meanwhile, complying with the principles of DOE ensures that the predictive model has excellent global fitting accuracy and reliable generalization capability. By combining the principle of randomization with the requirement of multiple sampling, we have achieved a precise characterization of complex physical field features while significantly reducing reliance on large-scale CFD simulations. Given the widespread application of surrogate models in structural parameter optimization [36,37], this study uses the trained RSM mapping function as the evaluation model for the objective function.

Then, the NSGA-II with elite strategy is adopted to jointly optimize the geometric parameters and flow velocity of the channel. To coordinate and balance the inherent contradiction between heat dissipation and pumping power consumption, the algorithm directly calls the trained RSM for efficient iteration. In addition, with the improved non-dominated sorting mechanism and crowding distance calculation, this algorithm can find Pareto optimal solution sets with physical significance in a large design space. Concomitantly, the system's built-in elite retention mechanism prevents the loss of Pareto non-dominated solutions during iterative optimization, ensuring that the algorithm always searches based

on existing optimal boundaries, thereby significantly improving the accuracy of convergence [38,39]. This automatic optimization framework, assisted by surrogate models, not only effectively avoids the high cost of large-scale CFD calculations but also achieves a comprehensive exploration of performance metrics, providing an efficient and reliable technical approach for identifying the optimal design solution for battery liquid-cooling systems.

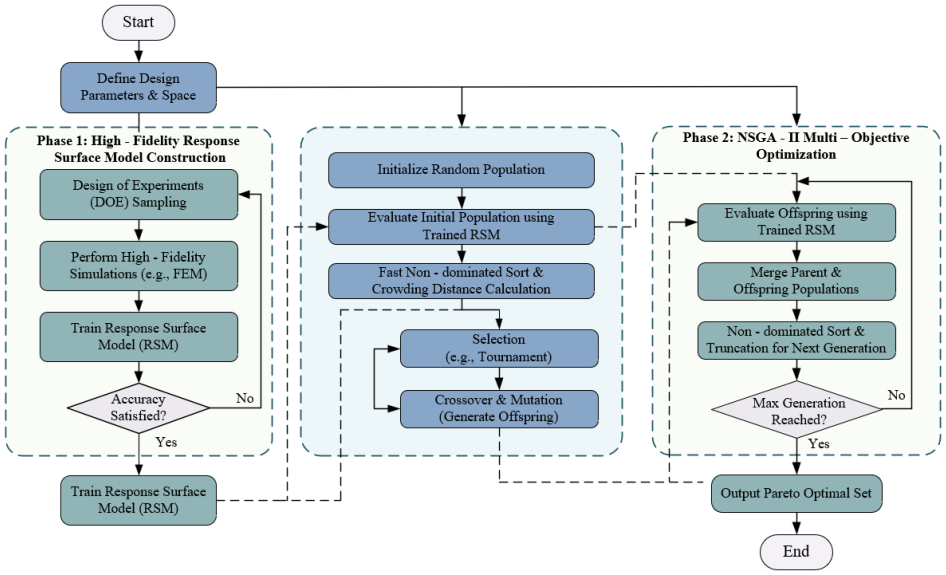


Figure 7. Integrated optimization architecture combining RSM surrogate modeling and the NSGA-II algorithm. Phase 1 defines the design space and validates model accuracy; Phase 2 executes the multi-objective evolutionary search based on the trained RSM to output the Pareto optimal set.

According to the geometric definition in Section 2.1, the design variables of this optimization framework are set as geometric parameters l, h, s, and inlet velocity v. In order to facilitate the establishment of a high-fidelity RSM model using the DOE method, this study defined the sampling intervals for these variables, and the specific optimization boundaries are detailed in Table 6.

Table 6. Range of parameter values used for the optimization design space.

Parameter (Unit)	Value Range
l (mm)	0.5–15
h (mm)	0.25–3
s (mm)	0.5–24
v (m/s)	0.01–0.5

Constructing an accurate RSM necessitates the scientific selection of sample points, as the optimization quality of the design space directly dictates the modeling fidelity. For the purpose of efficient modeling, the entire design space must be uniformly covered by a minimized number of points without compromising prediction accuracy. This study combines probability and statistics with the DOE method and uses the OLHS strategy to provide a robust solution to this demand. By optimizing the spatial dispersion, information entropy, extreme distance, and other indicators, the OLHS method not only realizes the uniform space-filling characteristics but also ensures the diversity of samples [40,41]. For the four key structural parameters, a total of 100 representative sample points are generated based on the strategy. Importantly, the initial 100 samples cover the design space of channel configurations on the same side (Case 1) and on the opposite side (Case 2). This comprehensive sampling ensures that subsequent optimization will not be biased towards a

specific layout. For the surrogate-model training dataset, all DOE samples were calculated in ANSYS Fluent under a 5 C discharge condition. The boundary conditions for these DOE cases were consistent with those described in Section 2.3. In addition, these DOE samples were calculated under steady-state conditions; therefore, no physical time-step size was required. The maximum temperature used for surrogate-model training was extracted from the converged steady-state temperature field as the highest temperature in the battery module (Table 7).

Table 7. List of representative sample data and simulation results.

Case	l (mm)	h (mm)	s (mm)	v (m/s)	P (Pa)	T (°C)
1	10.25	1.69	5.66	0.09	849.3	31.14
2	6.61	1.27	5.24	0.36	8745.2	27.38
3	10.61	1.84	7.66	0.16	1053.1	27.81
4	4.25	0.30	20.31	0.21	36,481.8	60.98
5	0.61	1.25	12.91	0.07	5552.7	153.02
6	8.13	0.64	9.77	0.40	5233.9	28.65
7	6.21	0.79	19.51	0.04	1109.3	75.66
8	0.91	1.67	15.53	0.48	23,045.1	36.39
9	12.66	0.54	20.05	0.36	12,332.6	27.51
10	14.49	0.69	18.43	0.34	7412.9	26.20
11	0.94	0.37	12.40	0.42	28,274.4	72.25
12	7.12	1.37	18.84	0.07	134.0	39.99
13	14.72	0.95	13.70	0.45	5021.4	26.83
14	4.99	0.79	13.48	0.20	6239.1	35.05
15	14.16	0.75	2.56	0.34	8988.7	26.81
16	3.08	1.10	5.12	0.06	3570.0	58.64
17	5.61	1.74	12.06	0.28	2597.7	29.12
18	6.07	1.33	21.99	0.14	1064.3	36.35
19	6.41	1.29	1.49	0.18	4710.1	52.71
20	2.59	0.68	11.68	0.08	5201.2	81.08
21	6.76	0.61	3.92	0.08	7597.0	47.37
22	2.05	1.52	0.90	0.04	5000.7	64.41
23	9.43	1.97	17.50	0.14	447.8	33.60
24	0.67	0.47	8.51	0.38	90,362.4	80.03
25	8.53	1.56	18.15	0.11	533.4	35.88
26	11.96	0.53	11.13	0.33	17,263.5	29.70
27	3.66	1.94	11.01	0.31	3837.7	30.49
28	6.91	1.60	1.98	0.41	10,307.2	25.59
29	3.31	0.73	19.16	0.14	4719.0	52.08
30	14.40	1.31	22.87	0.40	2188.5	32.41

It should be noted that some DOE samples exhibit extremely high maximum temperatures because they correspond to unfavorable parameter combinations with insufficient cooling capacity. These samples are retained in the dataset to ensure that the surrogate model can cover a wider design space and identify areas with insufficient cooling. However, they are not considered as physically acceptable final design solutions.

As shown in Figure 8, this study shows the steady-state thermal-hydraulic field distribution of Cases 1 to 3 to comprehensively verify the validity of the sampling data and the physical fidelity of the simulation model. From the pressure contours shown in Figure 8a–c, the hydrodynamic evolution shows an obvious stepped attenuation mode along the serpentine path. There is an obvious continuous pressure drop gradient from the high-pressure inlet to the low-pressure outlet. The isobars densely distributed at the channel turn (U-bend) show that the local flow resistance caused by fluid separation and wall friction is very significant. It is worth noting that Case 2 shows the most violent flow

resistance characteristics, with the maximum pressure drop reaching 8745.2 Pa; its narrow channel topology leads to an extremely steep pressure gradient, which is visually confirmed.

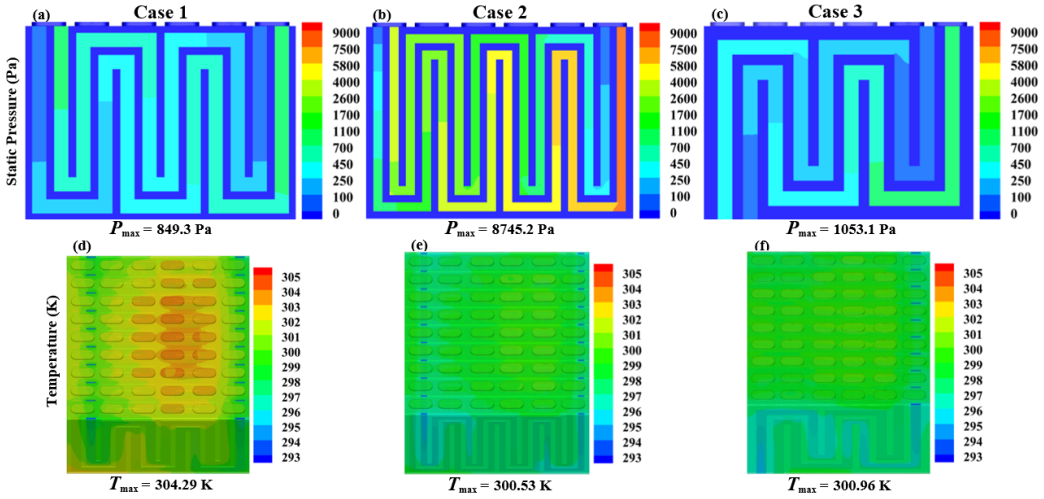


Figure 8. Steady-state thermal-hydraulic field distributions for Cases 1–3: (**a**–**c**) pressure contours showing hydrodynamic evolution; (**d**–**f**) temperature contours depicting heat accumulation.

As for the temperature field shown in Figure 8d–f, the cloud chart reveals a very uneven temperature distribution, which is characterized by an obvious gradient along the flow direction. It can be observed that the temperature increases monotonously along the coolant flow path, in which the "low-temperature zone" is strictly limited to the inlet area, while the "high-temperature zone" gradually expands to the outlet. This evolution marks the gradual saturation of the heat capacity of the coolant and leads to the corresponding weakening of the downstream convective heat transfer driving force. In addition, there is a significant transverse temperature gradient between adjacent channel strokes, and local hot spots mainly appear in the stagnant region at the corner of the channel and in the channel gap with low heat-dissipation efficiency. These temperature-field results indicate that, in addition to the maximum temperature, the temperature uniformity inside the battery module is also an important parameter affecting thermal safety performance. The maximum temperature records corresponding to the three Cases are 304.29 K, 300.53 K, and 300.96 K, respectively. This detailed observation and analysis confirms the high consistency between the visual physical gradient and the numerical results, and verifies that the proposed numerical Case can accurately capture the coupling mechanism of momentum transport and heat dissipation.

3. Results and Discussion

Aiming to achieve efficient exploration of battery thermal management systems, this study constructed an optimization framework using the modeFRONTIER 2020R3 platform, which enables the framework to have functions such as DOE, surrogate modeling, and sensitivity analysis. Using this framework, parameters l, h, s, and v are set as design variables, and pressure drop, P, and maximum temperature, T, are set as optimization objectives. Optimization is carried out while satisfying specific physical constraints, providing a foundation for effectively combining simulation data with optimization algorithms.

3.1. Training Response Surface Model

The construction of high-precision RSMs depends on the selection of mathematical regression algorithms with high matching accuracy, but different algorithms exhibit different predictive abilities when fitting complex thermohydraulic characteristics. Thus, in

this study, a comprehensive evaluation was conducted on nine different mathematical regression algorithms, including Gaussian Processes, Distributed Random Forest, Multilayer Perceptron, Shepard-K-Nearest, Radial Basis Functions, Smoothing Spline ANOVA, Stepwise Regression, Polynomial SVD, and Support Vector Regression. Seeking to effectively evaluate the predictive ability of the above surrogate models and prevent overfitting, this study introduced mean absolute error (MAE), mean absolute percentage error (MAPE), and coefficient of determination (R^2) to establish a comprehensive evaluation system. Through comparative analysis, the minimum error indices and the coefficient of determination closest to 1.0 were identified to screen for the optimal surrogate model.

According to the comparative analysis in Table 8, no single algorithm can achieve optimal prediction accuracy for two response targets simultaneously. Through comparative analysis, the Shepard-K-Nearest algorithm shows the best stability in handling highly nonlinear fluid pressure drops, with the highest R^2 value of 0.827 and the lowest MAE of 3740 Pa. In contrast, the Distributed Random Forest algorithm exhibits absolute fitting advantages in handling thermal responses dominated by heat conduction, reaching an R^2 value of 0.931 with an exceptionally low MAPE of 7.24%. Driven by the above error analysis, this study eschews the traditional single surrogate model prediction and instead uses a hybrid surrogate model.

Table 8. Comprehensive performance metrics (MAE, MAPE, and R^2) of different surrogate models for pressure drop and maximum temperature. The best-performing metrics for each objective are highlighted in bold.

Algorithm	Pressure Drop			Maximum Temperature		
	MAE (Pa)	MAPE (%)	R^2	MAE (°C)	MAPE (%)	R^2
Gaussian Processes	5120	208.0	0.770	10.60	24.2	0.155
Distributed Random Forest	6800	167.0	0.713	**2.79**	**7.24**	**0.931**
Multilayer Perceptron	6300	97.7	0.651	2.90	7.54	0.914
Shepard-K-Nearest	**3740**	**45.8**	**0.827**	5.85	13.0	0.807
Radial Basis Functions	4910	73.0	0.717	7.41	16.5	0.700
Smoothing Spline ANOVA	8340	147.0	0.437	4.20	9.47	0.887
Stepwise Regression	8350	110.0	0.491	10.10	21.3	0.283
Polynomial SVD	9240	310.0	0.443	9.18	24.1	0.430
Support Vector Regression	8610	170.0	0.463	7.42	20.1	0.589

In particular, the prediction accuracy of the pressure drop surrogate model is relatively low, mainly due to the wide range of pressure drop response changes and the limited number of training samples. The pressure drop is highly sensitive to the geometric structure of the flow channel and changes in the inlet flow velocity, which makes it difficult to fit the surrogate model. Therefore, the R^2 value of the best-performing pressure drop model is 0.827, and the MAE is 3740 Pa. Considering the overall variation characteristics of the pressure drop response, the prediction error is still within an acceptable range, and its impact on subsequent multi-objective optimization is limited.

Following the above error analysis, this study avoids using a traditional single-surrogate-model prediction strategy and instead adopts a hybrid surrogate model. More precisely, the Distributed Random Forest model was selected for predicting the maximum temperature, while the Shepard-K-Nearest model was used for predicting pressure drop. This method of selecting surrogate models for different optimization objectives effectively improves the accuracy of objective function evaluation. In the subsequent NSGA-II optimization process, approximately 5000 candidate solutions were predicted using a surrogate-model-assisted optimization framework, rather than being calculated directly through CFD. Accordingly, the computational cost during the optimization search

process has been significantly reduced, providing a foundation for efficiently obtaining a reliable Pareto optimal solution set.

A prediction dataset for the entire design space was generated using a hybrid surrogate model, and a sensitivity matrix was established based on it, as shown in Figure 9. This matrix quantifies the impact of design variables l, h, s, and v on system performance (system pressure drop P and maximum battery temperature T). Concerning hydraulic response, v and P show a strong positive correlation of 0.562. This trend can be explained by the flow resistance in the serpentine channel, where wall friction losses in the straight sections and local losses at the U-shaped bends together constitute the system pressure drop. As the inlet velocity increases, the wall shear stress and momentum loss at the bends become more significant, leading to an increase in the system pressure drop.

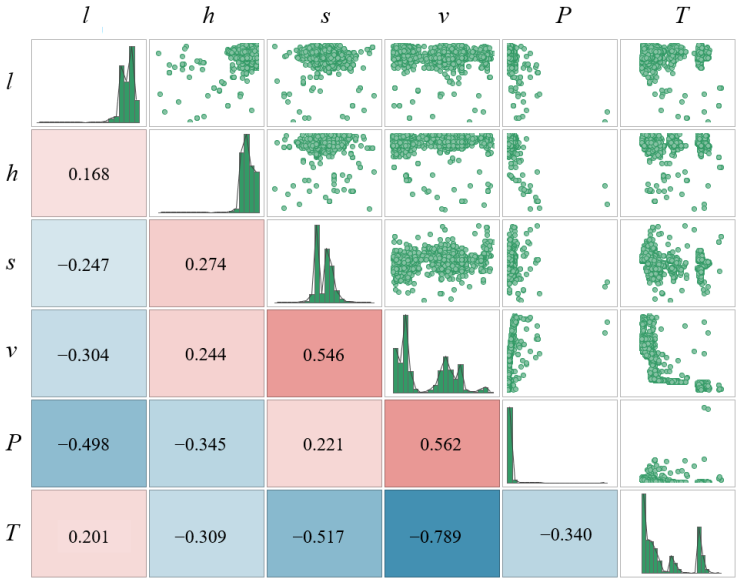


Figure 9. Sensitivity analysis and correlation map of the design parameters and objective functions.

For the thermal response, the inlet velocity v is the dominant factor affecting the maximum battery temperature T, with a negative correlation coefficient of -0.789. A higher inlet velocity increases the amount of coolant passing through the channel per unit time, which reduces the temperature rise of the coolant as it flows along the serpentine channel and enhances the overall cooling effect. Therefore, as v increases, the maximum battery temperature decreases. The channel spacing s is also negatively correlated with the maximum battery temperature, with a correlation coefficient of -0.517, indicating that within the current geometric range, channel distribution affects the cooling coverage and local heat accumulation on the battery surface. Compared with the inlet velocity, the influence of geometric parameters on temperature is not simply linear, but results from the combined effects of factors such as flow field distribution, heat transfer area, and heat accumulation in the downstream region of the channel.

By observing the interaction response of the objective function in the matrix, it can be found that there is a clear competitive feature between P and T. The negative correlation coefficient of -0.340 reveals the mutual conflict between targets, that is, increasing pressure drop is necessary at the cost of pursuing minimum temperature, which also provides support for the subsequent adoption of a multi-objective Pareto optimization process.

3.2. Multi-Objective Optimization and Pareto Frontier Analysis

In view of the significant competitive characteristics between system pressure drop and maximum battery temperature in the process of simultaneously seeking minimization, tra-

ditional single-objective conversion methods are often limited by the subjectivity of weight allocation and easily overlook the complex physical relationships between various objectives. In contrast, the multi-objective Pareto optimization strategy can comprehensively and objectively characterize the limit boundary of system performance by identifying the non-dominated solution set within the entire design space. Therefore, this study adopts the NSGA-II algorithm for multivariable global optimization, aiming to obtain the Pareto front and quantify the trade-off relationship between heat dissipation efficiency and pumping power consumption. However, the Pareto front contains a large number of mathematically equivalent non-dominated solutions, so additional evaluation criteria need to be introduced to evaluate and determine the final optimal design solution [42–44].

To determine the optimal solution from the Pareto non-dominated solution set, the evaluation criteria used need to have the ability to eliminate physical dimensional differences and objectively quantify the comprehensive benefits of each solution. For this purpose, this study adopted the TOPSIS method, which quantifies the Euclidean distance between each candidate solution and positive and negative ideal points to systematically evaluate the solutions [45,46]. In the attribute definition stage, both the system pressure drop and the maximum battery temperature are defined as cost-type objectives. These objectives need to be minimized. By calculating the relative closeness coefficient C_i^*, the optimal structural scheme can be ultimately determined from the Pareto front. The calculation formula is expressed as follows:

Dimensionless normalization of the decision matrix is performed first to eliminate the influence of different units between the system pressure drop and battery maximum temperature.

Equation (10) describes this normalization process, where x_{ij} and z_{ij} represent the original and normalized objective values for the j-th criterion of the i-th candidate solution, respectively:

$$z_{ij} = \frac{x_{ij}}{\sqrt{\sum_{i=1}^{m} x_{ij}^2}}, \tag{10}$$

Based on the objective attributes, the positive ideal solution (PIS) f^+ and the negative ideal solution (NIS) f^- are determined within the decision space. For the pressure drop, which serves as a cost-type indicator, f^+ and f^- are assigned the minimum and maximum values, respectively.

Euclidean distances D_i^+ and D_i^- from each candidate solution to the PIS and NIS are calculated using Equations (11) and (12):

$$D_i^+ = \sqrt{\sum_{j=1}^{n} w_j (z_{ij} - f_j^+)^2}, \tag{11}$$

$$D_i^- = \sqrt{\sum_{j=1}^{n} w_j (z_{ij} - f_j^-)^2}. \tag{12}$$

The weighting coefficients w_j are introduced to represent the relative importance of different optimization objectives in the TOPSIS decision-making process. The relative closeness C_i^* of each solution is subsequently determined via Equation (13):

$$C_i^* = \frac{D_i^-}{D_i^+ + D_i^-}. \tag{13}$$

The range of values for C_i^* is from 0 to 1, with values closer to 1 indicating that the design minimizes fluid pressure drop while ensuring efficient heat dissipation of the battery.

Considering that thermal safety is the primary requirement of battery thermal management systems, a higher weight is assigned to the maximum battery temperature in the TOPSIS decision-making process. Table 9 shows the TOPSIS decision results under temperature-priority weighting conditions. It can be seen that when the weighting combinations are w_P:w_T = 0.1:0.9 and 0.2:0.8, TOPSIS selects the same optimal structural parameter combination, indicating that the selected scheme remains stable under strong temperature-priority decision preferences. Compared with w_P:w_T = 0.1:0.9, w_P:w_T = 0.2:0.8 emphasizes thermal safety while still retaining a certain consideration of hydraulic resistance. Therefore, this study ultimately adopts w_P:w_T = 0.2:0.8 as the final weighting combination in the TOPSIS decision-making process.

Table 9. Sensitivity analysis of TOPSIS results under temperature-priority weighting factors.

w_P	w_T	C_i^*	l (mm)	s (mm)	h (mm)	v (m/s)	P (Pa)	T (°C)
0.1	0.9	0.8499	12.73	14.31	1.95	0.24	817.56	30.28
0.2	0.8	0.8077	12.73	14.31	1.95	0.24	817.56	30.28
0.3	0.7	0.7853	14.15	13.38	1.78	0.09	644.30	32.57
0.4	0.6	0.7831	13.58	10.99	1.74	0.07	332.37	42.54

The optimal solution determined by the TOPSIS decision-making tool is shown in Figure 10, with a system pressure drop of 817.56 Pa and a maximum battery temperature of 30.28 °C. The corresponding geometric parameters and inlet velocity are channel width of 12.73 mm, channel height of 1.95 mm, channel spacing of 14.31 mm, and inlet velocity of 0.24 m/s. It should be noted that although the inlet velocity is the dominant factor affecting the maximum temperature of the battery, the selected inlet velocity in the final optimization scheme is only 0.24 m/s, which is not close to the upper limit of the design range. This result indicates that the optimal solution does not simply rely on increasing the coolant velocity to reduce the maximum battery temperature, but rather strikes a balance between heat dissipation performance and pressure-drop reduction.

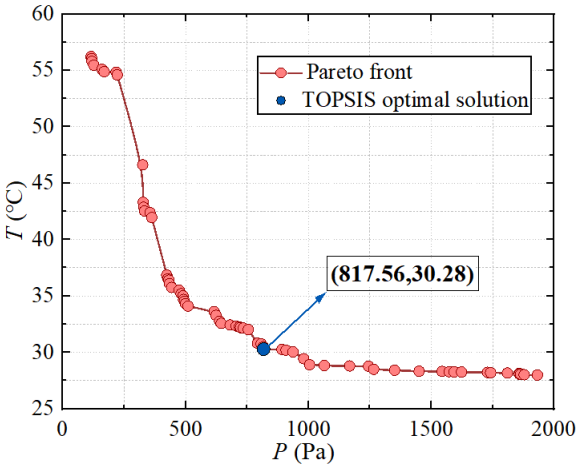


Figure 10. Pareto front of pressure drop vs. maximum temperature and the selected TOPSIS optimal solution.

3.3. Analysis of Optimization Results

Verification of the NSGA-II optimization results utilized a three-dimensional CFD model constructed from the optimal parameters selected via TOPSIS. From the temperature field shown in Figure 11c, the numerical simulation yields a maximum battery temperature of 30.07 °C or 303.22 K. Compared with the predicted 30.28 °C by RSM, the absolute deviation of this result is only 0.21 °C. Strictly limiting relative error within 0.69% not only

confirms the extremely high prediction fidelity of the surrogate model, but also proves the reliability of the optimized structure in terms of thermal safety. The performance of the flow field also confirms the above conclusion, as shown in Figure 11b. The simulated pressure drop of the system is 799.58 Pa, which is as low as 2.20% compared to the algorithm-predicted 817.56 Pa. The velocity streamline distribution shown in Figure 11a illustrates the flow details of the coolant. The ordered laminar flow mode not only reduces flow resistance but also minimizes flow separation at bends. In summary, the small numerical error and good heat dissipation effect jointly prove that this integrated optimization architecture can find the optimal solution from the multi-objective design space, providing reliable technical support for the development of power battery BTMS.

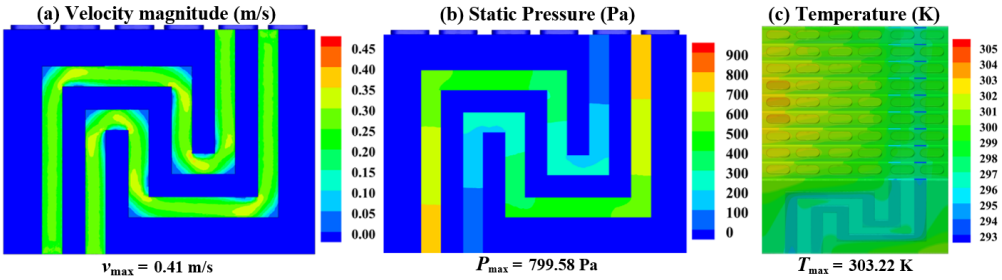


Figure 11. Multi-physical field distributions of the optimized configuration: (**a**) velocity streamlines; (**b**) static pressure; (**c**) temperature.

Based on the above verification results, this paper further evaluates the robustness of the proposed optimization framework from two aspects: numerical simulation and surrogate modeling. The grid-independence study and comparison with experimental data reported in [30] have reduced the uncertainty of the CFD-generated dataset, while comparing different surrogate models using MAE, MAPE, and R^2 ensures that the final surrogate models are selected based on their prediction accuracy. In addition, the selected optimal solution was further validated through CFD simulation, and the small deviation between the predicted results of the surrogate model and the CFD verification results indicates that the final optimized design has good reliability in the current design space.

Due to the relatively low inlet velocity of the optimized configuration, this study further calculated the Reynolds number (Re) of the coolant flow using the thermophysical properties of the 50% ethylene glycol aqueous solution. The Reynolds number under the optimized configuration was approximately 255.7, indicating that the coolant flow in the final optimized channel was in the laminar regime. It should be noted that the standard k-ϵ model was initially adopted to maintain a consistent numerical framework for the DOE database, in which the inlet velocity and serpentine channel geometry varied simultaneously within the design space. Some channel configurations contained repeated bends and local flow disturbances; therefore, a unified viscous-model setting was adopted during the surrogate-model training stage.

To evaluate the influence of viscous-model selection on the final optimization results, an additional laminar-flow simulation was performed for the optimal configuration. As shown in Figure 12, the velocity, pressure, and temperature distributions obtained using the laminar model were highly consistent with those predicted by the original turbulence model. The maximum system pressure drop changed from 799.58 Pa to 802.28 Pa, with a relative difference of only 0.34%. The maximum battery temperature changed from 303.22 K to 303.83 K, with a relative difference of 0.20%. These results indicate that although the optimized configuration was more appropriately characterized by laminar flow, the final pressure-drop and temperature predictions were only weakly affected by

the selected viscous model. Therefore, the main optimization conclusions of this study remained unchanged.

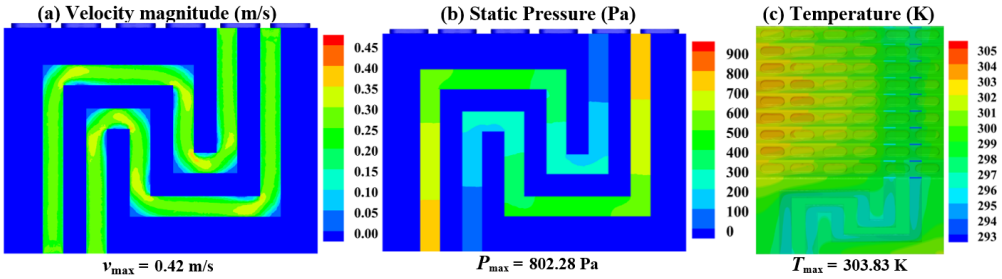


Figure 12. Simulated multiphysical field distributions obtained using the laminar model for comparison: (**a**) velocity magnitude; (**b**) static pressure; (**c**) temperature.

To further verify the thermal stability of the optimized structure, this study conducted three simulation scenarios on the system by increasing the inlet temperature in increments of 5 °C. As shown in Figure 13, when the inlet temperature rises from 25 °C to 35 °C, although the temperature level shifts proportionally overall, the basic heat distribution pattern remains unchanged. In addition, under extreme conditions with an inlet temperature of 35 °C, the structure can still limit the maximum temperature of the battery to 317.71 K, which corresponds to 44.56 °C. This result meets the temperature safety limit of 45 °C, confirming that the design has sufficient heat dissipation capability and thermal reliability in harsh environments.

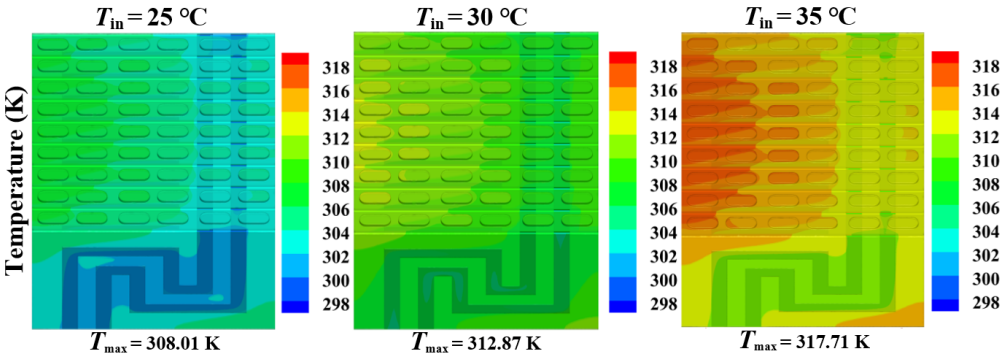


Figure 13. Steady-state temperature distributions of the optimized battery module under various coolant inlet temperatures (T_{in} = 25, 30 and 35 °C).

Figure 14 further details the transient temperature curves of the entire battery module at different inlet temperatures. Unlike the 1.5 C low-rate discharge behavior of a single cell shown in Figure 6, Figure 14 depicts the transient heat dissipation behavior at the module level. The rate of increase in the maximum temperature significantly decreases after about 400 s, indicating that the heat-dissipation rate of the liquid-cooled plate gradually approaches the heat-generation rate of the battery module. During the transient process, the coolant continues to flow through the internal channels of the liquid-cooled plate and constantly carries away the heat generated by the battery module. As the module temperature increases, the temperature difference between the battery module and the coolant increases, further enhancing the heat transfer between the solid structure and the flowing coolant. After about 400 s, the heat-generation rate of the battery module gradually approaches dynamic equilibrium with the heat-dissipation rate of the coolant, thereby suppressing the continuous increase in the maximum temperature. This phenomenon indicates that the optimized liquid-cooled plate has an effective heat-transfer capacity under the 5 C high-rate discharge condition.

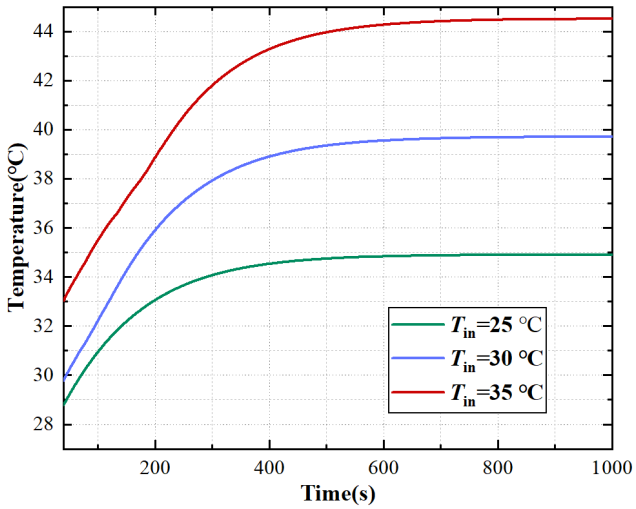


Figure 14. Transient temperature profiles of the maximum battery temperature for different T_{in} at 5 C discharge rate.

4. Conclusions

This study conducted structural optimization on the cooling system of EVs, and the main research results are summarized as follows:

1. By integrating OLHS with numerical simulation, a quantitative representation of the physical correspondence within the design space has been achieved. The results confirm that the hybrid surrogate model based on Shepard-K-Nearest and Distributed Random Forest has reasonable predictive capability in characterizing the nonlinear mapping relationship between pressure drop and battery temperature. The verification results indicate that the maximum relative error between the predicted values of the model and the numerical simulation values is limited to 2.2%, thereby providing a reliable computational foundation for the refined topology design of liquid-cooling systems.
2. Sensitivity analysis was conducted on the relationship between various parameters and optimization objectives, and the results showed that the inlet velocity v is the main cause of changes in battery temperature and system pressure drop. Increasing the inlet velocity v will lead to a decrease in temperature while increasing pressure drop, which constitutes the fundamental trade-off between heat dissipation efficiency and energy loss. In addition, the two optimization objectives exhibit different response logics to the geometric parameters of the flow channel. Although enlarging the channel dimensions significantly reduces the pressure drop, it shows a non-monotonic trend for temperature, which confirms the necessity of identifying the globally optimal geometric parameters through multi-objective optimization.
3. By combining the NSGA-II algorithm with TOPSIS decision analysis, the optimal parameter combination for performance was determined: the width of the channel was 12.73 mm, the height was 1.95 mm, the spacing was 14.31 mm, and the inlet flow velocity was 0.24 m/s. Under these conditions, the model predicted a pressure drop of 817.56 Pa and a maximum temperature of 30.28 °C. Fluent simulation verification showed that the simulated values for pressure drop and maximum temperature were 799.58 Pa and 30.07 °C, respectively. The small error between the two confirmed that the integrated optimization architecture has the ability to handle multi-objective optimization, and also demonstrated that the liquid-cooling plate with opposite-side layout has significant advantages in balancing heat dissipation gain and flow resistance loss.

From an engineering perspective, the results indicate that the improvement of cooling performance should not solely rely on increasing the inlet velocity. A moderate inlet velocity

combined with reasonable channel geometry is more conducive to balancing thermal safety and hydraulic resistance. The proposed CFD–surrogate-model-assisted optimization framework can be extended to other battery modules, but the specific geometric and flow parameters still need to be re-optimized according to the corresponding operating conditions. Future work will focus on conducting 5 C high-rate discharge experiments and incorporating the obtained data into a higher-precision optimization framework to enhance the system's prediction and optimization capabilities.

Author Contributions: S.M.: Methodology, Software, Writing—original draft, Investigation; Q.L.: Writing—review and editing, Software; W.L.: Conceptualization, Supervision; M.L.: Software, Data curation; X.H.: Visualization, Data curation. All authors have read and agreed to the published version of the manuscript.

Funding: This research was funded by Liaocheng University through the Doctoral Research Initiation Fund, grant number 318052334.

Data Availability Statement: Data will be made available on request.

Conflicts of Interest: The authors declare that they have no known competing financial interests or personal relationships that could have appeared to influence the work reported in this paper.

References

1. Farghali, M.; Osman, A.I.; Mohamed, I.M.A.; Chen, Z.; Chen, L.; Ihara, I.; Yap, P.S.; Rooney, D.W. Strategies to Save Energy in the Context of the Energy Crisis: A Review. *Environ. Chem. Lett.* **2023**, *21*, 2003–2039. [CrossRef]
2. Hassan, Q.; Viktor, P.; Al-Musawi, T.J.; Mahmood Ali, B.; Algburi, S.; Alzoubi, H.M.; Khudhair Al-Jiboory, A.; Zuhair Sameen, A.; Salman, H.M.; Jaszczur, M. The Renewable Energy Role in the Global Energy Transformations. *Renew. Energy Focus* **2024**, *48*, 100545. [CrossRef]
3. Gajdzik, B.; Wolniak, R.; Nagaj, R.; Žuromskaitė-Nagaj, B.; Grebski, W.W. The Influence of the Global Energy Crisis on Energy Efficiency: A Comprehensive Analysis. *Energies* **2024**, *17*, 947. [CrossRef]
4. Kim, T.; Song, W.; Son, D.Y.; Ono, L.K.; Qi, Y. Lithium-Ion Batteries: Outlook on Present, Future, and Hybridized Technologies. *J. Mater. Chem. A* **2019**, *7*, 2942–2964. [CrossRef]
5. Ding, Y.; Cano, Z.P.; Yu, A.; Lu, J.; Chen, Z. Automotive Li-Ion Batteries: Current Status and Future Perspectives. *Electrochem. Energy Rev.* **2019**, *2*, 1–28. [CrossRef]
6. Ramasubramanian, B.; Ling, J.; Jose, R.; Ramakrishna, S. Ten Major Challenges for Sustainable Lithium-Ion Batteries. *Cell Rep. Phys. Sci.* **2024**, *5*. [CrossRef]
7. Zhang, Q.; Yang, K.; Niu, J.; Liu, T.; Hu, J. Research on the Lower Explosion Limit of Thermal Runaway Gas in Lithium Batteries under High-Temperature and Slight Overcharge Conditions. *J. Energy Storage* **2024**, *79*, 109976. [CrossRef]
8. Micari, S.; Napoli, G. Electric Vehicles for a Flexible Energy System: Challenges and Opportunities. *Energies* **2024**, *17*, 5614. [CrossRef]
9. Gharehghani, A.; Rabiei, M.; Mehranfar, S.; Saeedipour, S.; Mahmoudzadeh Andwari, A.; García, A.; Reche, C.M. Progress in Battery Thermal Management Systems Technologies for Electric Vehicles. *Renew. Sustain. Energy Rev.* **2024**, *202*, 114654. [CrossRef]
10. Hwang, F.S.; Confrey, T.; Reidy, C.; Picovici, D.; Callaghan, D.; Culliton, D.; Nolan, C. Review of Battery Thermal Management Systems in Electric Vehicles. *Renew. Sustain. Energy Rev.* **2024**, *192*, 114171. [CrossRef]
11. Kirad, K.; Chaudhari, M. Design of Cell Spacing in Lithium-Ion Battery Module for Improvement in Cooling Performance of the Battery Thermal Management System. *J. Power Sources* **2021**, *481*, 229016. [CrossRef]
12. Feng, X.H.; Li, Z.Z.; Gu, F.S.; Zhang, M.L. Structural Design and Optimization of Air-Cooled Thermal Management System for Lithium-Ion Batteries Based on Discrete and Continuous Variables. *J. Energy Storage* **2024**, *86*, 111202. [CrossRef]
13. Moosavi, A.; Ljung, A.L.; Lundström, T.S. A Study on the Effect of Cell Spacing in Large-Scale Air-Cooled Battery Thermal Management Systems Using a Novel Modeling Approach. *J. Energy Storage* **2023**, *72*, 108418. [CrossRef]
14. Gao, C.; Song, K.; He, R.; Qi, Y.; Gu, B.; Su, M.; An, Z. Improving the Thermal-Hydraulic Performance of Air-Cooled Battery Thermal Management System by Flow Splitters. *J. Energy Storage* **2024**, *101*, 113818. [CrossRef]
15. Lyu, C.; Song, Y.; Wang, L.; Ge, Y.; Xiong, R.; Lan, T. A New Structure Optimization Method for Forced Air-Cooling System Based on the Simplified Multi-Physics Model. *Appl. Therm. Eng.* **2021**, *198*, 117455. [CrossRef]

16. Jiang, Y.; Smaisim, G.F.; Mahmoud, M.Z.; Li, Z.; Aybar, H.Ş.; Abed, A.M. Simultaneous Numerical Investigation of the Passive Use of Phase-Change Materials and the Active Use of a Nanofluid inside a Rectangular Duct in the Thermal Management of Lithium-Ion Batteries. *J. Power Sources* **2022**, *541*, 231610. [CrossRef]
17. Bao, Y.; Shao, S. Numerical Study on Ultrathin Wide Straight Flow Channel Cold Plate for Li-Ion Battery Thermal Management. *J. Energy Storage* **2023**, *64*, 107263. [CrossRef]
18. Zhang, Y.; Zuo, W.; E, J.; Li, J.; Li, Q.; Sun, K.; Zhou, K.; Zhang, G. Performance Comparison Between Straight Channel Cold Plate and Inclined Channel Cold Plate for Thermal Management of a Prismatic $LiFePO_4$ Battery. *Energy* **2022**, *248*, 123637. [CrossRef]
19. Kong, W.; Zhu, K.; Lu, X.; Jin, J.; Ni, M. Enhancement of Lithium-Ion Battery Thermal Management with the Divergent-Shaped Channel Cold Plate. *J. Energy Storage* **2021**, *42*, 103027. [CrossRef]
20. Kanjirakat, A.; Saldanha, R.; G. K., P.; Fernandes, D.V. Stereoscopic Serpentine Channel-Based Cold Plate Design for Enhanced Liquid Cooling of EV Batteries. *Battery Energy* **2026**, *5*, e70109. [CrossRef]
21. Liu, Z.; Xiong, C.; Du, X. Research on the Optimization Control Strategy of a Battery Thermal Management System Based on Serpentine Liquid Cooling Combined with Phase Change Material. *J. Power Sources* **2025**, *630*, 236127. [CrossRef]
22. Ding, Y.; Ji, H.; Wei, M.; Liu, R. Effect of Liquid Cooling System Structure on Lithium-Ion Battery Pack Temperature Fields. *Int. J. Heat Mass Transf.* **2022**, *183*, 122178. [CrossRef]
23. Zhao, D.; An, C.; Jia, Z.; Lei, Z. Structure Optimization of Liquid-Cooled Plate for Electric Vehicle Lithium-Ion Power Batteries. *Int. J. Therm. Sci.* **2024**, *195*, 108614. [CrossRef]
24. Fan, Y.; Wang, Z.; Fu, T.; Wu, H. Numerical Investigation on Lithium-Ion Battery Thermal Management Utilizing a Novel Tree-like Channel Liquid Cooling Plate Exchanger. *Int. J. Heat Mass Transf.* **2022**, *183*, 122143. [CrossRef]
25. Zhang, K.; Li, Y.; Chang, S.M.; Hu, L.; Wang, X.; Yu, M. Hydraulic and Thermal Performance Enhancement for the Cold Plate Using Topology Optimization. *Appl. Therm. Eng.* **2024**, *236*, 121829. [CrossRef]
26. Dai, H.; Tian, W.; Hou, M.; Liu, S.; Zhang, C.; Wei, Z.; Dong, Z.; Chin, C.S. Enhancing Thermal Management in Electric Commercial Vehicles: A Novel Liquid-Cooled Multiple Parallel-Serpentine Channels. *J. Energy Storage* **2025**, *107*, 114708. [CrossRef]
27. Fan, L.; Li, J.; Chen, Y.; Zhou, D.; Jiang, Z.; Sun, J. Study on the Cooling Performance of a New Secondary Flow Serpentine Liquid Cooling Plate Used for Lithium Battery Thermal Management. *Int. J. Heat Mass Transf.* **2024**, *218*, 124711. [CrossRef]
28. Vishwakarma, A.; Rana, U. Exploring Serpentine Cold-Plate Designs for Efficient Cooling of Li-ion Pouch Cells: A Computational Analysis. *Int. J. Heat Mass Transf.* **2025**, *244*, 126896. [CrossRef]
29. Mubashir, M.; Xu, J.; Guo, Z.; Wang, X.; Shi, C.; Mei, X. Experimental and Numerical Investigation of Single and Double Serpentine Channel Cold Plates on the Thermal Performance of Lithium Ion Pouch Battery. *J. Energy Storage* **2024**, *92*, 112200. [CrossRef]
30. Wu, B. Design and Optimization of Power Battery Heat Dissipation Structure Based on Microchannel Liquid Cooling Plate. Master's Thesis, Chongqing Jiaotong University, Chongqing, China, 2021. (In Chinese)
31. Dagnaw, E.S.; Aga, A.G.; Sufe, G. Energy Efficient Thermal and Hydraulic Performance Analysis of a Serpentine Liquid Cooled Lithium Ion Battery Pack for Electric Vehicles. *Sci. Rep.* **2026**, *16*, 16082. [CrossRef] [PubMed]
32. Niu, Z.h.; Pang, K.g.; Pang, B.b.; Wang, S. Orthogonal Experimental-Based Thermal Management Design and Simulation Optimization of a Liquid-Cooled Battery Module. *Sci. Rep.* **2025**, *15*, 33442. [CrossRef]
33. Launder, B.E.; Spalding, D.B. The Numerical Computation of Turbulent Flows. *Comput. Methods Appl. Mech. Eng.* **1974**, *3*, 269–289. [CrossRef]
34. Fan, X.; Meng, C.; Yang, Y.; Lin, J.; Li, W.; Zhao, Y.; Xie, S.; Jiang, C. Numerical Optimization of the Cooling Effect of a Bionic Fishbone Channel Liquid Cooling Plate for a Large Prismatic Lithium-Ion Battery Pack with High Discharge Rate. *J. Energy Storage* **2023**, *72*, 108239. [CrossRef]
35. Bernardi, D.; Pawlikowski, E.; Newman, J. A General Energy Balance for Battery Systems. *J. Electrochem. Soc.* **1985**, *132*, 5–12. [CrossRef]
36. Liao, J.; Ma, Q.; Hu, Y.; Zhang, Q.; Qiu, Y. CFD-assisted Multi-Objective Optimization of Burner for Enhanced DPF Regeneration Performance: Towards Cleaner Engine Emission. *Appl. Therm. Eng.* **2026**, *287*, 129417. [CrossRef]
37. Cheng, T.; Wang, P.; Liu, Q.; Wang, X.; Yang, B.; Mu, D. Performance Study of PEMFC Based on Response Surface Methodology and Optimization of Trapezoidal Block Parameters. *Energy Sources Part A Recovery Util. Environ. Eff.* **2025**, *47*, 2542962.
38. Li, Y.; Wang, G.; Chen, R.; Zhou, Y. Structural Optimization and Experimental Research of a High-Temperature Piezoelectric Force Sensor Based on AFSA-NSGA-II Fusion Algorithm. *Mech. Syst. Signal Process.* **2026**, *243*, 113736. [CrossRef]
39. Qin, L.; Lu, X.; Li, L.; Han, H.; Chai, M.; Yan, X.; Chen, S.; Wang, H.; Ma, W. Optimization of G1 Micromixer Structure in Two-Fluid Mixing Based on CFD and Response Surface Methodology. *Processes* **2024**, *12*, 122. [CrossRef]
40. Sun, Z.; Tang, F.; Shi, L.; Liu, H. Multi-Conditional Optimization of a High-Specific-Speed Axial Flow Pump Impeller Based on Machine Learning. *Machines* **2022**, *10*, 1037. [CrossRef]
41. Sun, C.; Lin, H.; Wu, Y.; Duan, Y. CFD-neural Network Collaborative Optimization Drives Aerodynamic Drag Reduction of Container Ship Fairings. *Ocean Eng.* **2025**, *342*, 122971. [CrossRef]

42. Liu, Q.; Sun, Q.; Wang, H.; Cheng, B. Multi-Objective Optimization of Automotive Power Battery Cooling Plate Structure Using Response Surface Methodology. *J. Mech. Sci. Technol.* **2024**, *38*, 6365–6374. [CrossRef]
43. Xu, L.; Lin, H.; Hu, N.; Xi, L.; Li, Y.; Gao, J. Multi-Objective Optimization Towards Heat Dissipation Performance of the New Tesla Valve Channels with Partitions in a Liquid-Cooled Plate. *Energies* **2024**, *17*, 3106. [CrossRef]
44. Dong, S.; Hu, P.; Zhang, C.; Hu, X.; Zhuang, W.; Wu, D. How to Optimally Design Industrial High-Temperature Heat Pump for Multiple Objectives and Working Conditions? *Energy* **2025**, *329*, 136830. [CrossRef]
45. Shi, H.; Liu, M.; Li, Y.; Wang, S.; Qiu, C.; Cheng, M.; Yuan, J.; Yang, K.; Kang, C. Multi-Objective Optimization of Integrated Lithium-Ion Battery Thermal Management System. *Appl. Therm. Eng.* **2023**, *223*, 119991. [CrossRef]
46. Arulselvan, S.; Veera Ajay, C.; Michael Thomas Rex, F.; Maharajan, S. Optimization and Modelling of Tribological Properties in Self-Lubricating AA2024/Nano-Graphene/Nano-WC Hybrid Composites Using RSM-CCD, TOPSIS, Pareto Analysis and ANFIS. *Proc. Inst. Mech. Eng. Part C J. Mech. Eng. Sci.* **2025**, *239*, 9780–9799. [CrossRef]

Disclaimer/Publisher's Note: The statements, opinions and data contained in all publications are solely those of the individual author(s) and contributor(s) and not of MDPI and/or the editor(s). MDPI and/or the editor(s) disclaim responsibility for any injury to people or property resulting from any ideas, methods, instructions or products referred to in the content.